

# Journal of Materials Chemistry A

Accepted Manuscript



This is an *Accepted Manuscript*, which has been through the Royal Society of Chemistry peer review process and has been accepted for publication.

*Accepted Manuscripts* are published online shortly after acceptance, before technical editing, formatting and proof reading. Using this free service, authors can make their results available to the community, in citable form, before we publish the edited article. We will replace this *Accepted Manuscript* with the edited and formatted *Advance Article* as soon as it is available.

You can find more information about *Accepted Manuscripts* in the [Information for Authors](#).

Please note that technical editing may introduce minor changes to the text and/or graphics, which may alter content. The journal's standard [Terms & Conditions](#) and the [Ethical guidelines](#) still apply. In no event shall the Royal Society of Chemistry be held responsible for any errors or omissions in this *Accepted Manuscript* or any consequences arising from the use of any information it contains.

# Tailored SrTiO<sub>3</sub>/TiO<sub>2</sub> Heterostructures for Dye-Sensitized Solar Cells with Enhanced Photoelectric Conversion Performance

Enyan Guo, Longwei Yin\*

*Key Laboratory for Liquid-Solid Structural Evolution and Processing of Materials, Ministry of Education, School of Materials Science and Engineering, Shandong University, Jinan 250061, P. R. China*

\*To whom correspondence should be addressed. Tel.: + 86 531 88396970. Fax: + 86 531 88396970. E-mail: [yinlw@sdu.edu.cn](mailto:yinlw@sdu.edu.cn)

**Abstract** We present a novel type of SrTiO<sub>3</sub>/TiO<sub>2</sub> nanosheet heterostructures via a facile hydrothermal process, with a tunable microstructure, phase component and surface area by adjusting the molar ratio of Sr and Ti precursors. The synthesized SrTiO<sub>3</sub>/TiO<sub>2</sub> heterostructure nanostructures can provide a high surface area and porous structure for improving dye loading capacity and hence the amount of photogenerated charges contributing to the photocurrent. The formation of heterostructures between SrTiO<sub>3</sub> and TiO<sub>2</sub> with a uniquely matched band gap energy structure can efficiently separate photogenerated charge carriers. Photoluminescence emission and electrochemical impedance spectroscopy (EIS), incident photon-to-electron conversion efficiency (IPCE) measurements reveal a lower recombination rate of photogenerated electrons and holes, and a longer electron lifetime for the DSSCs based on the SrTiO<sub>3</sub>/TiO<sub>2</sub> heterostructures. The photoelectric conversion efficiency and short-circuit current density of DSSCs based on SrTiO<sub>3</sub>/TiO<sub>2</sub> heterostructures are greatly enhanced over that of pure TiO<sub>2</sub> nanosheets. DSSCs based on the SrTiO<sub>3</sub>/TiO<sub>2</sub> heterostructures shows a highest short-circuit current density of 12.55 mAcm<sup>-2</sup> and a maximal photoelectric conversion efficiency of 7.42% under one sun illumination.

**Keywords:** TiO<sub>2</sub> nanosheets, heterostructure, perovskite SrTiO<sub>3</sub>, dye-sensitized solar cells, band gap

## 1. Introduction

Among third-generation photovoltaic devices, dye-sensitized solar cells (DSSCs) have been recognized as one of the most promising alternatives for low-cost and high solar-to-electricity energy conversion efficiency due to their low cost and possible fabrication of flexible solar cells.<sup>1-7</sup> In the past decades, considerable efforts have been made on novel sensitizers,<sup>8-10</sup> electrolytes,<sup>11,12</sup> photoanodes<sup>13-16</sup> to improve the power conversion efficiency and long-term stability of DSSCs.<sup>2</sup> The structural design of the photoelectrode plays a key issue in improving cell performance, which depends mainly on the light harvesting capacities related to the dye adsorbing ability, surface area, porous microstructures, and the band gap energy property of the photoelectrodes. Among various oxide semiconductors, nanocrystalline TiO<sub>2</sub> has proven to be one of the most suitable materials for solar energy conversion in view of its outstanding properties, such as suitable band position, non-toxicity, low cost, chemical and photonic stability, and biocompatibility.<sup>17</sup> Since the morphology, crystal structure and size of TiO<sub>2</sub> are crucial factors in determining its chemical, optical and electrochemical performances, variety of structured TiO<sub>2</sub>, such as nanoparticles,<sup>18</sup> nanosheets,<sup>19</sup> nanotubes,<sup>20</sup> nanowires,<sup>21</sup> and nanospheres<sup>22</sup> have been fabricated and applied to the photoanode for DSSCs. Among all kinds of morphologies, porous and two-dimensional TiO<sub>2</sub> nanosheets have attracted widespread attention due to their high-surface area and porous structure which are favorable for more dye adsorption and charge separation.<sup>23-25</sup>

Nevertheless, TiO<sub>2</sub> as an intrinsic semiconductor has a common predicament with lower quantum efficiency leading to poor photocatalytic activity. This is due to the rapid recombination of photogenerated electron-hole pairs, which greatly decreases the photocatalytic efficiency in decomposing organic pollutants and photo-electrical conversion efficiency in solar cells.<sup>26</sup> It is well-documented that charge separation of photogenerated electrons and holes is required for high performance DSSCs. Several attempts have been made to enhance photoelectric conversion performance by suppressing recombination of photogenerated electron-hole pairs via coupling of semiconductors such as PbS,<sup>27</sup> SnO<sub>2</sub>,<sup>28</sup> ZnO,<sup>29</sup> Nb<sub>2</sub>O<sub>5</sub>,<sup>30</sup> and CdS<sup>31</sup> with TiO<sub>2</sub>. Recently, DSSCs based on TiO<sub>2</sub> nanosheets as photoanode have attracted much attention.<sup>19</sup> The photoelectric conversion efficiency of DSSCs based on Au nanoparticles loaded TiO<sub>2</sub> nanosheets is proven to be greatly enhanced.<sup>32</sup> DSSCs based on TiO<sub>2</sub> photoanode with gradient structure in nanosheet/nanoparticle film exhibits an enhanced photoelectric conversion efficiency of 6.48%, exceeding that of pure nanoparticle-based DSSCs.<sup>19</sup>

SrTiO<sub>3</sub>, as a well-known uniquely perovskite structured semiconductor, has attracted considerable attention. SrTiO<sub>3</sub> offers favorable energetics for photocatalysis since its conduction band edge is 200 mV more negative than that of TiO<sub>2</sub>.<sup>33</sup> This makes SrTiO<sub>3</sub> a good candidate for coupling with TiO<sub>2</sub> to improve photo-electrochemical performance. In this regard, a proper combination of SrTiO<sub>3</sub> with TiO<sub>2</sub> can lead to improving not only electron transfer ability from the conduction band of SrTiO<sub>3</sub> to that of TiO<sub>2</sub>, but also hole transfer kinetics from the valence band of TiO<sub>2</sub> to that of SrTiO<sub>3</sub>. Some researchers investigated the photocatalytic performance and related mechanism of SrTiO<sub>3</sub>/TiO<sub>2</sub> photocatalysts, suggesting that the coupled SrTiO<sub>3</sub>/TiO<sub>2</sub> composite could improve the charge separation and achieve a higher photocatalytic activity.<sup>34-37</sup> For example, heterostructured TiO<sub>2</sub>/SrTiO<sub>3</sub> nanotube array photocatalysts display enhanced photocatalytic properties compared with pure TiO<sub>2</sub> nanotube arrays in decolorizing methylene blue in aqueous solution.<sup>38</sup> Zhu's study on

the SrTiO<sub>3</sub>/TiO<sub>2</sub> composite film presents a higher separation efficiency of the photogenerated electron-hole pairs, achieving a good photocathodic protection effect on stainless steel.<sup>39</sup>

Importantly, the enhanced charge separation effect between photo-induced generated electrons and holes of SrTiO<sub>3</sub>/TiO<sub>2</sub> heterostructures is expected to improve the photoelectric conversion efficiency of DSSCs based on the SrTiO<sub>3</sub>/TiO<sub>2</sub> heterostructures.<sup>40</sup> Compared with the study of SrTiO<sub>3</sub>/TiO<sub>2</sub> heterostructured catalysts for photocatalytically decolorizing and degrading organic pollutants, only few works are reported on the photovoltaic performance based on SrTiO<sub>3</sub>/TiO<sub>2</sub> heterostructure photoanodes. Song et al.<sup>41, 42</sup> synthesized a tailored SrTiO<sub>3</sub>-TiO<sub>2</sub> porous spherical heterostructures, demonstrating an enhanced photoelectric conversion efficiency. Recently, Zhang et al.<sup>43</sup> reported that coupling SrTiO<sub>3</sub> with TiO<sub>2</sub> nanotubes can provide synergetic effects for achieving better charge separation and thus producing improved photocurrent and photovoltage in a photoelectrochemical cell. While the solar cell based on SrTiO<sub>3</sub>-TiO<sub>2</sub> nanoporous heterostructures, displays an overall conversion efficiency increase from 3.81 for TiO<sub>2</sub> to 4.39% for SrTiO<sub>3</sub>-TiO<sub>2</sub> heterostructures.<sup>44</sup> The study by Hu's group suggests that the power conversion efficiency of radio frequency magnetron sputtering synthesized SrTiO<sub>3</sub>-modified TiO<sub>2</sub> thin film electrodes can be enhanced to 5.91% from 4.78% for pure TiO<sub>2</sub> electrode.<sup>45</sup>

However, the synthesis of large surface area SrTiO<sub>3</sub>/TiO<sub>2</sub> nanosheet heterostructure with a controlled substitution of Sr into lattice of TiO<sub>2</sub> nanosheets is greatly challenging and important to obtain promising photoelectric conversion efficiency. Furthermore, the relation between the charge separation behavior, the optical emission and adsorption performance, and the photoelectric conversion performance needs to be investigated. In this study, SrTiO<sub>3</sub>/TiO<sub>2</sub> heterostructures with a novel nanostructure were prepared by a two-step hydrothermal method for the first time. Controlled substitution of Sr into TiO<sub>2</sub> nanosheets to form the novel SrTiO<sub>3</sub>/TiO<sub>2</sub> nanosheet heterostructure provides us with a mean to examine the influence of content of SrTiO<sub>3</sub> in improving the photoelectrical conversion performance. The microstructure of the unique SrTiO<sub>3</sub>/TiO<sub>2</sub> heterostructures can be tuned by adjusting the molar ratio of Sr and Ti precursors.

The synthesized SrTiO<sub>3</sub>/TiO<sub>2</sub> heterostructure nanostructures can provide a high surface area for dye loading, and a uniquely matched band gap energy structure between SrTiO<sub>3</sub> and TiO<sub>2</sub> for the SrTiO<sub>3</sub>/TiO<sub>2</sub> heterostructures can efficiently separate photogenerated charge carriers. Photoluminescence emission and electrochemical impedance spectroscopy (EIS) measurements reveal a lower recombination rate of photogenerated electrons and holes, and longer electron lifetime for DSSCs based on the SrTiO<sub>3</sub>/TiO<sub>2</sub> heterostructures. The photoelectric conversion efficiency and short-circuit current density of DSSCs based on SrTiO<sub>3</sub>/TiO<sub>2</sub> heterostructures is greatly enhanced. DSSCs based on the SrTiO<sub>3</sub>/TiO<sub>2</sub> heterostructures shows a highest short-circuit current density of 12.55 mAcm<sup>-2</sup> and a maximal photoelectric conversion efficiency of 7.42% under one sun illumination. Comparing with the conversion efficiency of 5.45%, with a short-circuit current density of 9.17 mAcm<sup>-2</sup> for DSSCs based on pure TiO<sub>2</sub> nanosheets, the photoelectric conversion performance is greatly improved.

## 2. Experimental

### 2.1 Preparation of SrTiO<sub>3</sub>/TiO<sub>2</sub> Heterostructure Nanocrystals.

**Synthesis of TiO<sub>2</sub> Nanosheets:** A typical anatase TiO<sub>2</sub> nanosheet was prepared by a hydrothermal method.<sup>46</sup> A 10 mL titanium butoxide (Ti(OC<sub>4</sub>H<sub>9</sub>)<sub>4</sub>) was transferred in a Teflon-lined 50 mL autoclave at ambient temperature, followed by the addition of 1.2 mL hydrofluoric acid solution (49 weight %) under stirring, and the reaction was kept at 200 °C for 24 h. Then the resulted white TiO<sub>2</sub> precipitates were centrifuged and washed with ultra-pure water and ethanol for several times, and finally the obtained samples (designated as TiO<sub>2</sub> nanosheets T1) were dried at 50 °C for 24 h.

**Fabrication of SrTiO<sub>3</sub>/TiO<sub>2</sub> Heterostructure Nanocrystals:** The obtained TiO<sub>2</sub> nanosheets acted not only as a structure-directed template but also as the Ti source for the production of SrTiO<sub>3</sub>. In a typical procedure, 60 mL of Sr(OH)<sub>2</sub> solution (10 mM) was transferred to a Teflon-lined (90 mL) autoclave, followed by the addition of TiO<sub>2</sub> nanosheets under stirring at ambient temperature. After stirring for 30 min, the autoclave was sealed and kept at 180 °C for 18 h. After reaction, the resultant products were centrifuged, thoroughly washed with 0.1 M HCl and ultra-pure water several times, and lastly dried in air at room temperature. Corresponding to an adjustable Sr/Ti molar ratio of 1/4, 2/4, 3/4, 4/4, 6/4 according to the initial amount of raw materials, the obtained SrTiO<sub>3</sub>/TiO<sub>2</sub> heterostructure samples are denoted as ST0, ST1, ST2, ST3, ST4, respectively.

## 2.2 Solar cell fabrication.

**Preparation of SrTiO<sub>3</sub>/TiO<sub>2</sub> Photoanodes:** To prepare the photoanode of SrTiO<sub>3</sub>/TiO<sub>2</sub> heterostructure nanocrystals, fluorine doped tin oxide (FTO) glass as transparent conducting glass (FTO glass, 15Ω<sup>-1</sup>) was cleaned by sonication in soapy water, acetone and ethanol for 20 min during each washing step. Firstly, the blocking layer solution was created by treating with an aqueous solution of TiCl<sub>4</sub> (40 mM) at 60 °C for 15 min to retard interfacial recombination between electrons in the highly conducting FTO and the I<sup>3-</sup> oxidized electrolyte.<sup>47</sup> Secondly, a layer of SrTiO<sub>3</sub>/TiO<sub>2</sub> paste was spin-coated onto the FTO glass plates by the spin coating method at the speed of 2000 rpm for 30 seconds. The thickness of photoanode is about 10 μm obtained by repetitive spinning for several times. The paste fabrication process is as follows:<sup>48</sup> Briefly, a 10wt% ethyl cellulose solution contains 0.12 g ethyl cellulose powders and 10.8 g ethanol. The solution was injected into another suspension (0.2 g of SrTiO<sub>3</sub>/TiO<sub>2</sub> power and 0.8 g of terpineol which was diluted with 1.0 mL of ethanol). Then, the mixture suspension was stirred in an agate mortar and sonicated for three consecutive times; the two steps were both kept 20 min. Finally, a heating process (dried at 125 °C for 10 min, and gradually heated under flowing air at 325 °C for 5 min, at 375 °C for 5 min, at 450 °C for 15 min and 500 °C for 15 min) was carried on to remove the polymer template and organic compounds.

**Fabrication of DSSCs:** The annealed electrodes were sensitized by immersing into a 5×10<sup>-4</sup> M N-719 (Cis-diisothocyanato-bis(2,2'-bipyridyl-4,4'-dicarboxylato) ruthenium (II) bis (tetrabutylammonium)) dye solution dissolved in equal volumes of acetonitrile (Aladdin-reagent, China) and *tert*-butanol (Aladdin-reagent, China) at ambient temperature for 24 h, followed by washing with acetonitrile to remove non-chemisorbed dye, and dried before being assembled in solar cells. The Pt counter electrodes were prepared by coating with a drop of 0.01 M H<sub>2</sub>PtCl<sub>6</sub> ethanol solution on the cleaned FTO glass and sintered at 400 °C for 15 min. The two electrodes were thermally sealed together with a 25 μm thick Surlyn polymer seal (Surlyn, DuPont) into a sandwich type cell. The electrolyte (electrolyte of 0.6 M 1-methy-3-propylimidazolium iodide (PMII), 0.05 M

LiI, 0.05 M I<sub>2</sub>, and 0.5 M 4-tertbutylpyridine (TBP) in a (85:15 vol %) mixture of acetonitrile (Aladdin-reagent, China) and valeronitrile (Aladdin-reagent, China) was injected through a hole in the counter electrode of the assembled cell and driven into the cell via vacuum backfilling. The hole was sealed using another piece of slide glass-backed Surlyn.

### 2.3 Characterization.

The composition and crystal structure of the obtained nanocrystals were examined by an X-ray diffractometer (Philips Rigaku D/Max-kA X-ray diffractometer equipped with a Cu K $\alpha$  source at 40 kV and 30 mA). The surface morphology of as-prepared samples was analyzed by SU-70 field-emission scanning electron microscopy (FESEM). The detailed microstructure of the synthesized product was analyzed by using a Phillips Tecnai 20U-Twin high-resolution transmission electron microscope and attached X-ray energy dispersive spectrometry (EDS) at an acceleration voltage of 200 kV. The surface area of the samples was evaluated by the Brunauer-Emmett-Teller (BET) method using N<sub>2</sub> physisorption analysis at 77 K with a Gold APP V-Sorb 2800P. Porosity distributions were calculated from the adsorption branch of isotherm using the corrected form of the Kelvin equation by means of the Barrette Joynere Halenda (BJH) method. Prior to physisorption, the samples were degassed at 160 °C under vacuum for 3 h. X-Ray photoelectron spectroscopy (XPS) measurements of the material binding energy distributions were carried out in a Thermo Scientific ESCALAB250 spectrometer.

Absorption spectra were recorded with a TU-1901 spectrophotometer to obtain the information about the band gap energy of the as-synthesized nanocrystals. Dye uptake content per unit area (1 cm<sup>2</sup>) was investigated using UV-vis spectroscopy (TU-1901) by the dissolution of dye adsorbed the sample films membrane in 0.2 M NaOH water and ethanol (50:50, v/v) solution.<sup>20</sup> The photoluminescence (PL) spectra were recorded using conventional spectrometers (Cary-50, Varian Co.). Current–voltage characteristics under simulated AM 1.5 illumination were measured using a solar simulator (Newport, Class 3A, 94023A) at one sun (AM1.5G, 100 mW cm<sup>-2</sup>) by a Keithley 2420 source meter equipped, and light intensity was measured using a calibrated Si solar cell (certificated by NREL). The photoactive area of 0.16 cm<sup>2</sup> was defined by a black metal mask slightly larger than the active area to cut off stray light.<sup>49</sup> The electrochemical impedance spectroscopy (EIS) measurements were performed using a Princeton Parstate 2273A in a two-electrode design; the photoanode served as a working electrode and the Pt-coated on FTO as a counter electrode at an applied bias of the open circuit voltage under one-sun irradiation. The frequency range of 100 mHz~100 kHz with an AC voltage magnitude of 10 mV. The EIS data were analyzed with an appropriate equivalent circuit using simulation software.

## 3. Results and discussion

### 3.1. Structure characterization

The crystal structures of the SrTiO<sub>3</sub>/TiO<sub>2</sub> heterostructures are determined by X-ray diffraction (XRD) patterns (Fig. 1). Fig. 1a shows the XRD pattern of pure TiO<sub>2</sub> (T1), all diffraction peaks can be indexed to anatase TiO<sub>2</sub> (JCPDS: 21-1272). For the SrTiO<sub>3</sub>/TiO<sub>2</sub> heterostructures (Fig. 1b-d), there are two series of peaks, one type can be attributed to anatase TiO<sub>2</sub>, another can be well assigned to cubic SrTiO<sub>3</sub> (JCPDS 35-0734). Furthermore, it is clearly shown that with the molar ratio of Sr/Ti increasing, the peak intensity of TiO<sub>2</sub> phase becomes smaller, while the peak intensity of SrTiO<sub>3</sub> phase gets stronger. As the ratio of Sr/Ti is up to 6/4, the diffraction peaks

related to anatase  $\text{TiO}_2$  disappear (see Fig. S1b). It is shown that we can tune the microstructure and phase components by adjusting the molar ratio of Si/Ti. When the content of molar ratio of Sr/Ti for precursors is lower than 6/4, the synthesized products is composed of anatase  $\text{TiO}_2$  and cubic  $\text{SrTiO}_3$ , and as the molar ratio of Sr/Ti is larger than 6/4, only cubic  $\text{SrTiO}_3$  can be obtained.

The morphology of the as-prepared  $\text{TiO}_2$  and  $\text{SrTiO}_3/\text{TiO}_2$  heterostructure samples synthesized in different Sr/Ti molar ratios is examined by FESEM (Fig. 2). Fig. 2a-b shows FE-SEM images of T1 sample hydrothermally synthesized at 200 °C for 24 h. The low SEM image in Fig. 2a reveals a well-defined sheet-shaped structure with a rectangular outline with a side length of 100-120 nm.<sup>46</sup> Magnified SEM image in Fig. 2b shows a rough surface characteristic for the  $\text{TiO}_2$  nanosheet sample. The rough structures can increase the surface area of the sample, providing much favorable space for dye loading.  $\text{SrTiO}_3/\text{TiO}_2$  heterostructure nanocrystals are easily synthesized by heating the mixture of  $\text{TiO}_2$  nanosheets and strontium hydroxide octahydrate solution at 180 °C for 18 h under the hydrothermal condition. As revealed in Fig. 2c-d, at a low Sr/Ti molar ratio of 2/4, the as-prepared  $\text{SrTiO}_3/\text{TiO}_2$  heterostructure nanosheets (ST1) remain the same morphology and structures as that of pure  $\text{TiO}_2$  nanosheet. As the Sr/Ti molar ratio increases to 4/4, the synthesized ST3 sample is mainly composed of cubes with relatively large thickness, a small amount of thin nanosheets can also be observed among the cube-like products, as shown in Fig. 2e-f.

Fig. 3 depicts transmission electron microscopy (TEM) images of ST1 heterostructure. From low magnification TEM images in Fig. 3a-b, it is suggested that the products are composed of uniformly nanosheets and some fine nanoparticles homogeneously distributed among the nanosheet matrix. The nanosheets display a size of 100-102 nm, while the fine nanoparticles show an average size of only 1-2 nm. Fig. 3c depicts a typical high resolution TEM lattice image of the products showing the hybrids of nanosheet and nanoparticle. The marked d-spacing of 0.27 nm for a nanoparticle is in well agreement with that of (110) plane of cubic  $\text{SrTiO}_3$ , while the marked d-spacing of 0.23 nm and 0.24 nm in the lattice image for the nanosheet corresponds well with d-spacing of (-112) and (01-3) planes of anatase  $\text{TiO}_2$ , respectively. The electron diffraction (ED) pattern reveals the phase components of the ST1 samples (Fig. 3d), with the diffraction rings corresponding well with that of (101), (200), (215), (303) planes of anatase  $\text{TiO}_2$ , and (110), (111), (211), (220), (311), (303) planes of cubic  $\text{SrTiO}_3$ , respectively. It is clearly illustrated that the nanoparticle is cubic  $\text{SrTiO}_3$  and the nanosheets are anatase  $\text{TiO}_2$ .

For the T1 sample of pure  $\text{TiO}_2$  nanosheets, Fig. 4a and Fig. 4b depict two typical low-magnification TEM images obtained from different views. The as-prepared  $\text{TiO}_2$  nanosheets sample (T1) shows a side length of 100-120 nm (Fig. 4a). Fig. 4b depicts a typical side-viewed TEM image of  $\text{TiO}_2$  nanosheets, indicating an average thickness of 5 nm for the  $\text{TiO}_2$  nanosheets. Fig. 4c demonstrates a HRTEM lattice image of a single  $\text{TiO}_2$  nanosheet. The marked d-spacing of 0.35 nm corresponds well to that of (101) plane of anatase  $\text{TiO}_2$ . Fig. 4d is a typical ED pattern from the pure  $\text{TiO}_2$  nanosheets, the diffraction rings corresponding to the (101), (004), (200), (211), (204) planes of anatase  $\text{TiO}_2$ , respectively.

From low magnification TEM image of ST3 sample in Fig. 4e, it is shown that as the Sr/Ti molar ratio is 4/4, the synthesized ST3 sample is mainly composed of  $\text{SrTiO}_3$  cubes, and also a small amount of  $\text{TiO}_2$  nanosheets,

in good agreement with above XRD results. The SrTiO<sub>3</sub> cubes show a cube-like morphology with a size of 100×80 nm. The fringe spacing of 0.35 nm in Fig. 4f corresponds to d-spacing of (101) plane of anatase TiO<sub>2</sub> nanosheet. While, the fringe spacing of 0.27 nm in Fig. 4g matches well with d-spacing of (110) plane of cubic SrTiO<sub>3</sub>. ED pattern in Fig. 4h clearly shows that the ST3 sample is composed of cubic SrTiO<sub>3</sub> and anatase TiO<sub>2</sub>, with diffraction rings corresponding well with (101), (200) planes of anatase TiO<sub>2</sub>, and (110), (111), (211) planes of cubic SrTiO<sub>3</sub>, respectively.

X-ray energy dispersive spectrometry (EDS) results for different samples are shown in Fig. S2. EDS data of the heterostructure materials suggest that the samples were composed of Sr, Ti, and O elements. The actual molar ratio of Sr/Ti in the prepared samples is 15%, 43%, 75%, 86% and 98%, corresponding to the samples ST0, ST1, ST2, ST3 and ST4, respectively. It is obviously shown that the actual molar ratio of Sr/Ti obtained is slightly lower than the theoretical value of each sample (Table S1 and inset of Fig. S2). Also, EDS data reveal that only Ti and O constituents for pure TiO<sub>2</sub> nanosheets. Cu peak is from the TEM grid used to support the samples.

Scheme 1 illustrates the formation process of SrTiO<sub>3</sub>/TiO<sub>2</sub> heterostructures. It is shown that this unique heterostructure is a result of a dissolution-precipitation mechanism.<sup>50</sup> After the growth of TiO<sub>2</sub> nanosheets, TiO<sub>2</sub> nanosheets were put into the alkaline solution to react with Sr<sup>2+</sup> ions of strontium hydroxide octahydrate [Sr(OH)<sub>2</sub>·8H<sub>2</sub>O]. The morphology, crystal structure, and phase components can be tuned by adjusting the molar ratio of Sr/Ti. As the molar ratio of Sr/Ti is low, fine nanoparticles of SrTiO<sub>3</sub> can nucleate and grow on TiO<sub>2</sub> nanosheet to form SrTiO<sub>3</sub>/TiO<sub>2</sub> heterostructure.<sup>51,52</sup> With the molar ratio of Sr/Ti further increasing, more SrTiO<sub>3</sub> nanocrystals are formed through the reaction of TiO<sub>2</sub> with Sr(OH)<sub>2</sub>, the TiO<sub>2</sub> nanosheets are gradually depleted, and SrTiO<sub>3</sub> nanocrystals grow and assemble into cube-like crystals.<sup>53-55</sup> As increasing the molar ratio of Sr/Ti to 6/4, pure SrTiO<sub>3</sub> cube-like structures are obtained.

The chemical composition and chemical bonding structure of SrTiO<sub>3</sub>/TiO<sub>2</sub> heterostructures (ST1) are investigated using the X-ray photoelectron spectroscopy (XPS). According to XPS analysis, the relative Sr/Ti atomic percent of the ST1 sample is determined to be 8.80/18.08=49%. The result is in agreement with the EDS data. The general survey spectra in Fig. 5a indicate the existence of Ti, Sr and O elements in the ST1 sample. The high-resolution spectrum of the Ti 2p shown in Fig. 5b suggests that the characteristic peaks centered at 458.33 eV (Ti 2p<sub>3/2</sub>) and 464.09 eV (Ti 2p<sub>1/2</sub>), indicating a Ti<sup>4+</sup> oxidation state in the SrTiO<sub>3</sub>/TiO<sub>2</sub> heterostructure.<sup>56, 57</sup> The XPS spectrum of Sr 3d region can be deconvoluted into two peaks of Sr 3d<sub>5/2</sub> and Sr 3d<sub>3/2</sub> centered at 132.74 and 134.47 eV, respectively (Fig. 5c). The peak at 132.74 eV is in accordance with those reported for perovskite SrTiO<sub>3</sub>, and the energy peak at 134.47 eV can be attributed to SrO complexes.<sup>40, 58</sup> The XPS spectral peak of O1s shows two small peaks, (Fig. 5d) one centered at 529.56 eV should be associated with TiO<sub>2</sub> and SrTiO<sub>3</sub>, whereas another peak centered at 531.78 eV is believed to be related to the adsorbed oxygen such as carbonates and hydroxyl oxides.<sup>55, 58</sup>

Table 1 Structural property of TiO<sub>2</sub> nanosheets and SrTiO<sub>3</sub>/TiO<sub>2</sub> samples

Samples	BET surface area /m <sup>2</sup> g <sup>-1</sup>	Pore diameter /nm	Total pore volume /cm <sup>3</sup> g <sup>-1</sup>
T1	76.69	27.48	0.689
ST0	72.43	27.09	0.682
ST1	68.92	30.28	0.649
ST2	49.43	32.36	0.499
ST3	25.10	29.63	0.257
ST4	16.66	37.66	0.209

The textural properties of specific surface area, pore size distribution, pore volume of TiO<sub>2</sub> nanosheets and SrTiO<sub>3</sub>/TiO<sub>2</sub> heterostructures prepared under different molar ratios of Sr/Ti of ST0, ST1, ST2, ST3 and ST4 samples are characterized using the nitrogen adsorption-desorption isotherms (Fig. 6). For pure TiO<sub>2</sub> nanosheet sample (T1), it shows a type III isotherm (based on IUPAC classification) with a smooth capillary condensation step occurred at a relative pressure of (P/P<sub>0</sub> ≈ 0.90-1.0) and H3 type hysteresis loops, indicating their relatively large pore size and a large specific surface area. This is due to the presence of large amounts of pores between the TiO<sub>2</sub> nanosheets, and also probably caused by the crevice hole within TiO<sub>2</sub> nanosheets. While the SrTiO<sub>3</sub>/TiO<sub>2</sub> heterostructures display still type III isotherms, with a smooth capillary condensation step occurred at high relative pressures (P/P<sub>0</sub> ≈ 0.9-1.0) and H3 type hysteresis loops. The textural parameters such as specific surface area, pore diameter and pore volume of TiO<sub>2</sub> nanosheets and SrTiO<sub>3</sub>/TiO<sub>2</sub> heterostructure materials, are summarized in Table 1. As revealed in Table 1, sample ST0 has a specific surface area of 72.43 m<sup>2</sup> g<sup>-1</sup> and a pore size distribution centered at 27.09 nm. With the molar ratio of Sr/Ti increasing, the surface area decreases to 68.92 m<sup>2</sup> g<sup>-1</sup> for ST1 and 16.66 m<sup>2</sup> g<sup>-1</sup> for ST4 sample from 76.69 m<sup>2</sup> g<sup>-1</sup> for T1 sample, and the pore size decreases to 27.09 nm for ST0 sample, and increases to 37.66 nm for ST4 sample from 27.48 nm for T1 sample.

### 3.2 The performance of solar cells

The photovoltaic activity of DSSCs is closely related with the lifetime of photogenerated electrons and holes. Photoluminescence emission signals (PL) result from the recombination of photoinduced charge carriers. To describe the charge separation behavior and efficiency in the samples, PL spectra of (a) T1, (b) ST0, (c) ST1, (d) ST2, (e) ST3 and (f) ST4 samples are comparatively investigated, as shown in Fig. 7. The PL emission spectrum is obtained by a spectrophotometer containing a xenon lamp with 360 nm excitation wavelength. All the samples display a broad-band emission from 360 to 440 nm with a similar emission peak at 390 nm. The pure TiO<sub>2</sub> (T1) and SrTiO<sub>3</sub> samples display relatively stronger emission compared with ST0, ST1, ST2, and ST3 samples. Generally, the emission peak intensity of the SrTiO<sub>3</sub>/TiO<sub>2</sub> heterostructures increase with the molar ratio of Sr/Ti increasing. The ST1 heterostructure sample shows the weakest PL emission at about 390 nm among the SrTiO<sub>3</sub>/TiO<sub>2</sub> heterostructure samples, indicating the lowest recombination rate of photogenerated electrons and holes, with the longest lifetime of photogenerated electrons and holes.

Comparison of J-V characteristics of DSSCs based on T1, ST0, ST1, ST2, ST3, and ST4 electrodes is shown in Fig. 8. The inset in Fig. 8 suggests that the thickness of the film is around 10  $\mu\text{m}$ . Open-circuit photovoltage ( $V_{oc}$ ), short-circuit photocurrent density ( $J_{sc}$ ), fill factor of the cell (FF), power conversion efficiency ( $\eta$ ), and dye adsorption are listed in Table 2. The capacity of dye loading exerts a profound influence on the photocurrent density for DSSCs,<sup>20</sup> in order to estimate the amount of adsorbed N719 dyes by measuring the eluted dye molecules from  $\text{SrTiO}_3/\text{TiO}_2$  heterostructures with UV-vis absorption spectroscopy. It is worth noting that the dye concentration is 102.62  $\text{nmol cm}^{-2}$  for T1, 97.02  $\text{nmol cm}^{-2}$  for ST0, 93.83  $\text{nmol cm}^{-2}$  for ST1, 65.15  $\text{nmol cm}^{-2}$  for ST2, 36.39  $\text{nmol cm}^{-2}$  for ST3, and 24.51  $\text{nmol cm}^{-2}$  for ST4, respectively. The results suggest that the ST0 sample had 1.03 times higher dye adsorption than the ST1 sample, while it was 3.96 times for the ST4 sample. As shown in Table 1, the decreased surface area of  $\text{SrTiO}_3/\text{TiO}_2$  heterostructures was a direct consequence of the weakened dye loading capacity.

The open-circuit photovoltage ( $V_{oc}$ ) keeps an increasing trend with the increase of molar ratio of Sr/Ti for  $\text{SrTiO}_3/\text{TiO}_2$  heterostructures. The DSSCs based on T1 shows the lowest  $V_{oc}$  due to the intrinsic property (band gap = 3.2 eV) of  $\text{TiO}_2$  pure nanosheets, also the highest fill factor (FF) value is obtained for T1 sample due to pure  $\text{TiO}_2$  nanosheet film showing better contact with the FTO glass substrate, resulting in lower contact resistance. The ST1 sample display the highest FF value among the  $\text{SrTiO}_3/\text{TiO}_2$  heterostructure samples. With the molar ratio of Sr/Ti ranging from 1/4 to 6/4 (ST0 to ST4), the short-circuit photocurrent density ( $J_{sc}$ ) first increases from 10.95  $\text{mA cm}^{-2}$  (ST0), to a maximum value of 12.55  $\text{mA cm}^{-2}$  at (ST1), and then decreases gradually with further increasing the molar ratio of Sr/Ti. The power conversion efficiency ( $\eta$ ) and short-circuit photocurrent density ( $J_{sc}$ ) displays a decreasing trend with the molar ratio of Sr/Ti increasing. For example, DSSCs based on ST2 heterostructure with a molar ration of 3/4 for Sr/Ti shows the highest short-circuit current density of 10.22  $\text{mA cm}^{-2}$  and a photoelectric conversion efficiency of 5.68%. While DSSCs based on ST1 heterostructure shows the highest short-circuit current density of 12.55  $\text{mA cm}^{-2}$  and a maximal photoelectric conversion efficiency of 7.42%. Compared with the conversion efficiency of 5.45% and short-circuit current density of 9.17  $\text{mA cm}^{-2}$  for DSSCs based on pure  $\text{TiO}_2$  nanosheet sample (T1), the conversion efficiency and short-circuit current density of DSSCs based on ST1 sample is increased by 36% and 37%, respectively.

Table 2 Performances of solar cells based on (a) T1, (b) ST0, (c) ST1, (d) ST2, (e) ST3 and (f) ST4 samples under simulated AM 1.5 illuminations.

Samples	$V_{oc}$ (mV)	$J_{sc}$ ( $\text{mA cm}^{-2}$ )	Fill Factor (%)	$\eta^a$ (%)	Dye adsorption ( $\text{nmol cm}^{-2}$ )
T1	739	9.17	80.27	5.45	102.62
ST0	767	10.95	68.69	5.77	97.02
ST1	776	12.55	76.82	7.42	93.83
ST2	780	10.22	71.30	5.68	65.15
ST3	782	6.94	62.91	3.36	36.39
ST4	804	5.03	66.14	2.66	24.51

a)  $\eta$  (%) =  $J_{sc} V_{oc} FF / P_{in}$ , where  $P_{in} = 100 \text{ mW cm}^{-2}$  (AM 1.5). Each  $\eta$  is an average value obtained from six

samples.

The incident photon-to-electron conversion efficiency (IPCE) is more pertinent than UV-vis absorption/reflection for studying the photocurrent generation of DSSCs. The corresponding IPCE spectra of all the samples are shown in Fig. 9, which is in good agreement with the conversion efficiency of the solar cells (Table 2 and Fig. 8). IPCE spectra do not shift significantly for the different samples, which is consistent with their UV-vis diffuse reflectance spectra. Clearly, the maximum IPCE increases, reaches a maximum at sample ST1 and then decreases with the increase of Sr content, having the same trend with the variation of  $J_{sc}$ .

Table 3 Series resistances and electron lifetime of the typical samples based DSSCs

Samples	$R_s$ ( $\Omega$ )	$R_{ct1}$ ( $\Omega$ )	$R_{ct2}$ ( $\Omega$ )	$R_{diff}$ ( $\Omega$ )	Frequency (Hz)	$\tau_e$ (ms)
T1	16.41	9.96	52.30	5.56	20	7.96
ST1	16.83	11.40	22.18	8.60	10.08	15.79
ST3	17.32	13.59	119.39	10.38	63.10	2.52
ST4	17.89	12.64	133.43	7.39	158.86	1.00

To better understand the interfacial reaction of photoexcited electrons and the effect of film structure on the photovoltaic performance of DSSCs, the electrochemical impedance spectroscopy (EIS) measurements were performed to reveal the electron transport kinetics during the photovoltaic process of DSSCs.<sup>59,60</sup> Fig. 10a shows the Nyquist plots of DSSCs based on T1, ST1, ST3, and ST4 film electrodes. The equivalent circuit is shown as the inset in Fig. 10a using non-linear-least-square (NLLS) fit analysis software (Zview software) and the fitting data are given in Table 3.  $R_s$  can be recognized and fitted according to an equivalent circuit model as the sheet resistance of the FTO glass substrate and the contact resistance at FTO/TiO<sub>2</sub>(SrTiO<sub>3</sub>/TiO<sub>2</sub>) interface.<sup>61</sup> The  $R_s$  values of DSSCs based on T1, ST1, ST3, and ST4 electrodes calculated according to the equivalent circuit are 16.41, 16.83, 17.32, and 17.89  $\Omega$ , respectively. It is clear that  $R_s$  of T1 and ST1 electrodes is smaller than that of ST3 and ST4 electrodes, implying better electronic contact between TiO<sub>2</sub>/FTO, ST1/ FTO than that of the interface between ST3/FTO, ST4/FTO glass. The small semicircle in the high frequency region is related to the charge transfer resistance ( $R_{ct1}$ ) and interfacial capacitance ( $CPE_1$ ) at interface between the electrolyte and Pt electrode.<sup>62</sup> The electron transport resistance ( $R_{ct2}$ ) at intermediate frequency and interfacial capacitance ( $CPE_2$ ) give information on the impedance at the TiO<sub>2</sub> (SrTiO<sub>3</sub>/TiO<sub>2</sub>)/electrolyte interfaces,<sup>63</sup> while this at low-frequency on behalf of the impedance ( $R_{diff}$ ) is related to the finite diffusion of the electrolyte.<sup>64</sup> In particular, the electron transport resistance ( $R_{ct2}$ ) plays a vital role in the photovoltaic performance of DSSCs in that it is related to the number of electrons going back to the electrolyte at the SrTiO<sub>3</sub>-TiO<sub>2</sub>/electrolyte interface.<sup>63</sup> The  $R_{ct2}$  values of DSSCs based on T1, ST1, ST3, and ST4 electrodes calculated according to the equivalent circuit are 52.30, 22.18, 119.39, and 133.43  $\Omega$ , respectively. It is clearly that the  $R_{ct2}$  of ST1 electrode is the smallest, indicating high charge transport ability at the ST1 photoanode.

Bode phase plots of the EIS can offer the lifetime information of electrons during the photovoltaic process and

are shown in Fig. 10b. According to the EIS model developed by Kern *et al.*,<sup>64</sup> the electron lifetime ( $\tau_e$ ) can be calculated according to the equation  $\tau_e = 1/2\pi f_{\max}$ , where  $f_{\max}$  is the maximum frequency of the peak in the intermediate frequency region.<sup>65</sup> The  $\tau_e$  values of DSSCs based on T1, ST1, ST3, and ST4 electrodes are calculated to be 7.96, 15.79, 2.52, and 1.00 ms, respectively. The larger value of  $\tau_e$  means the lower recombination rate of electrons and holes during the electron transfer across the working film, in good agreement with the result of electron transport resistance ( $R_{ct2}$ ). Longer electron lifetimes are observed for DSSCs based on ST1 electrodes, indicating more effective suppression of the back-reaction of the injected electrons with the  $I_3^-$  ions in the electrolyte.

The proposed charge transfer process in SrTiO<sub>3</sub>/TiO<sub>2</sub> heterostructures is illustrated in Scheme 2. TiO<sub>2</sub> is a kind of wide bandgap semiconductor (3.2 eV) with its valence band (2.91 V vs NHE) and conduction band (-0.29 V vs NHE); both the conduction band and valence band of TiO<sub>2</sub> are more negative than the valence band (2.14 V vs NHE) and conduction band (-1.26 V vs NHE) of SrTiO<sub>3</sub>. The good matching of band edges between TiO<sub>2</sub> and SrTiO<sub>3</sub> is important to form a type II heterojunction. Under UV irradiation, electrons photogenerated from the conduction band of SrTiO<sub>3</sub> pass to the lower lying conduction band of TiO<sub>2</sub>, while the photogenerated holes in the valence band of TiO<sub>2</sub> transfer oppositely to that of SrTiO<sub>3</sub>. The simultaneous transfer of electrons and holes in the SrTiO<sub>3</sub>/TiO<sub>2</sub> system increases the spatial separation of charge carriers, and thus reduces the probability of recombination.<sup>66</sup> Furthermore; it is the close contact between TiO<sub>2</sub> and SrTiO<sub>3</sub> that the separation efficiency of photogenerated electrons and holes would be maximized. In other words, if the content of SrTiO<sub>3</sub> is too large, the charge transfer activity and charge separation ability will be reduced. Thus, the recombination of photogenerated electrons and holes was prevented effectively thus benefiting the higher photocatalytic efficiency of the ST1 sample than the other samples. So the optimized ratio of Sr/Ti for SrTiO<sub>3</sub>/TiO<sub>2</sub> heterostructure is 2/4.<sup>67</sup>

On the basis of the above experimental results, the highest power conversion efficiency of the DSSCs based on ST1 electrodes can be attributed to the effects of three factors: firstly, the SrTiO<sub>3</sub>/TiO<sub>2</sub> heterostructure nanocrystals has higher light absorbing ability for enhancing the utilization of solar light, which are confirmed by the UV-vis diffuse reflectance measurements (Fig. S3). Secondly, the capacity of dye absorbing exerts a profound influence on the photocurrent density, the relatively higher specific surface area and presence of large amounts of pores in SrTiO<sub>3</sub>/TiO<sub>2</sub> heterostructure nanosheets (ST1) is in favor of high dye absorption ability. Thirdly, the electron transport resistance ( $R_{ct2}$ ) of ST1 electrode is the smallest, which results in lower contact resistance and higher photocurrent density. Furthermore, as illustrated in Scheme 2, the matched bandgap structure of SrTiO<sub>3</sub>/TiO<sub>2</sub> heterostructures (ST1) is beneficial for the simultaneous transfer of electrons and holes, which increases the spatial separation of charge carriers, and thus reduces the probability of recombination of electrons and holes. The good spatial separation of charge carriers can also be demonstrated by the ST1 heterostructure sample shows the weakest emission, indicating the lowest recombination rate of photogenerated electrons and holes, with the longest lifetime of photogenerated electrons and holes. The maximum IPCE appears at sample ST1, which can be a good description of high light-harvesting efficiency, electron injection efficiency from excited dye molecules to TiO<sub>2</sub>, and electron collection efficiency at the anode. Electrochemical

impedance spectroscopy (EIS) also reveals a lower recombination rate of photogenerated electrons and holes, and a longer electron lifetime for the DSSCs based on the SrTiO<sub>3</sub>/TiO<sub>2</sub> heterostructures.

Although several works about DSSCs based on the TiO<sub>2</sub>/SrTiO<sub>3</sub> heterostructure photoanodes are previously reported, it is still greatly challenging to develop a TiO<sub>2</sub>/SrTiO<sub>3</sub> heterostructure in a controlled way. Huang et al. recently reported a situ hydrothermal synthesis of SrTiO<sub>3</sub>/TiO<sub>2</sub> heterostructure nanosheets to enhance photocatalytic degradation activity, showing that the photocatalytic activity of TiO<sub>2</sub> nanosheets on degradation of RhB is enhanced by coupling SrTiO<sub>3</sub>.<sup>68</sup> Compared with the Huang's work, the present DSSCs based on SrTiO<sub>3</sub>/TiO<sub>2</sub> nanosheet heterostructures shows a superior photoelectric conversion performance than the previously reported DSSCs based on SrTiO<sub>3</sub>/TiO<sub>2</sub> heterostructures, with a short-circuit current density of 12.55 mAcm<sup>-2</sup> and a maximal photoelectric conversion efficiency of 7.42% under one sun illumination. Controlled substitution of Sr into TiO<sub>2</sub> nanosheets to form the novel TiO<sub>2</sub>/SrTiO<sub>3</sub> heterostructure provides us with an effective mean to examine the influence of SrTiO<sub>3</sub> in improving the photoelectric conversion performance of the TiO<sub>2</sub>/SrTiO<sub>3</sub> heterostructured photoanodes for DSSCs. Compared with the reported conversion efficiency of DSSCs based on other types of SrTiO<sub>3</sub>/TiO<sub>2</sub> heterostructures<sup>38-40</sup>, the photoelectric conversion performance is greatly improved. The work reported here provides a novel heterostructures with a structural advantage and with a uniquely matched band gap energy structure that can efficiently separate photogenerated charge carriers. The synthesized SrTiO<sub>3</sub>/TiO<sub>2</sub> heterostructure nanostructures display a high surface area and porous structure for improving dye loading capacity and hence the amount of photogenerated charges contributing to the photocurrent.

The photoelectric conversion performance of the SrTiO<sub>3</sub>/TiO<sub>2</sub> heterostructure can be comparable with previously reported works. For example, as bare TiO<sub>2</sub> nanotubes and heterostructured SrTiO<sub>3</sub>-TiO<sub>2</sub> nanotubes are applied as photoanodes in DSSCs, a photoconversion efficiency of 0.18% and 0.48% can be achieved, respectively.<sup>41</sup> For the core-shell nanoporous SrTiO<sub>3</sub>/TiO<sub>2</sub> heterostructured photoanodes for DSSCs, an overall conversion efficiency of 4.39% can be obtained, higher than the efficiency of 3.81 for pure TiO<sub>2</sub> photoanode.<sup>44</sup> The study by Hu's group suggests that the power conversion efficiency of SrTiO<sub>3</sub>-modified TiO<sub>2</sub> electrodes can be enhanced to 5.91% from 4.78% for pure TiO<sub>2</sub> electrode.<sup>45</sup> It is obviously that we have obtained the excellent photoelectric conversion performance of DSSCs based on the tailored SrTiO<sub>3</sub>/TiO<sub>2</sub> nanosheet heterostructured photoanodes. The unique heterostructures with high specific surface area suppresses the recombination rate of photogenerated electron-hole pairs, and prolongs the carrier lifetime of photo-induced electrons and holes, demonstrating greatly enhanced photoelectric conversion efficiency.

#### 4 Conclusions

In summary, a novel type of SrTiO<sub>3</sub>/TiO<sub>2</sub> heterostructures was successfully synthesized by a facile two-step hydrothermal process for the first time. The microstructure and phase components of the heterostructure products can be tuned by adjusting the molar ratio of Sr and Ti precursors. DSSCs based on the ST1 photoanode exhibits the highest conversion efficiency of 7.42% and fill factor of 76.82% under one sun illumination. The performance improvement of solar cells can be attributed to the strong light absorbing ability of SrTiO<sub>3</sub>/TiO<sub>2</sub>

heterostructure nanosheets, the strong uptake ability of dye molecule due to the larger surface area and porous structure characteristics, and the electron transported facilitated by the heterojunctions.

#### **Acknowledgment**

We acknowledge support from the National Natural Science Funds for Distinguished Young Scholars (No.: 51025211), National Nature Science Foundation of China (No.: 51472148, 51272137), the Tai Shan Scholar Foundation of Shandong Province.

#### **Supporting Information**

XRD patterns, EDS spectra and UV-vis diffuse reflectance spectra (DRS) of  $\text{TiO}_2$  and  $\text{SrTiO}_3/\text{TiO}_2$  samples.

## References

1. O'Regan, B.; Gratzel, M., *Nature* **1991**, *353*, 737–740.
2. Yella, A.; Lee, H. W.; Tsao, H. N.; Yi, C.; Chandiran, A. K.; Nazeeruddin, M. K.; Diao, E. W.; Yeh, C. Y.; Zakeeruddin, S. M.; Gratzel, M., *Science* **2011**, *334*, 629–634.
3. Santra, P. K.; Kamat, P. V., *J. Am. Chem. Soc.* **2012**, *134*, 2508–2511.
4. Im, J. H.; Lee, C. R.; Lee, J. W.; Park, S. W.; Park, N. G., *Nanoscale* **2011**, *3*, 4088–4093.
5. Fu, Y. P.; Peng, M.; Lv, Z. B.; Cai, X.; Hou, S. C.; Wu, H. W.; Yu, X.; Kafafy, H.; Zou, D. C., *Nano Energy* **2013**, *2*, 537–544.
6. Wu, J. H.; Xiao, Y. M.; Tang, Q. W.; Yue, G. T.; Lin, J. M.; Huang, M. L.; Huang, Y. F.; Fan, L. Q.; Lan, Z.; Yin, S.; Sato, T., *Adv. Mater.* **2012**, *24*, 1884–1888.
7. Liu, B.; Aydil, E. S., *J. Am. Chem. Soc.* **2009**, *131*, 3985–3990.
8. Nazeeruddin, M. K.; Kay, A.; Rodicio, I.; Humphry-Baker, R.; Mueller, E.; Liska, P.; Vlachopoulos, N.; Graetzel, M., *J. Am. Chem. Soc.* **1993**, *115*, 6382–6390.
9. Kim, S.; Lee, J. K.; Kang, S. O.; Ko, J.; Yum, J. H.; Fantacci, S.; De Angelis, F.; Di Censo, D.; Nazeeruddin, M. K.; Grätzel, M., *J. Am. Chem. Soc.* **2006**, *128*, 16701–16707.
10. Gao, F.; Wang, Y.; Shi, D.; Zhang, J.; Wang, M.; Jing, X.; Humphry-Baker, R.; Wang, P.; Zakeeruddin, S. M.; Grätzel, M., *J. Am. Chem. Soc.* **2008**, *130*, 10720–10728.
11. Wang, M. K.; Chamberland, N.; Breau, L.; Moser, J. E.; Humphry-Baker, R.; Marsan, B.; Zakeeruddin, S. M.; Gratzel, M., *Nat. Chem.* **2010**, *2*, 385–389.
12. Wang, H.; Zhang, X.; Gong, F.; Zhou, G.; Wang, Z. S., *Adv. Mater.* **2012**, *24*, 121–124.
13. Law, M.; Greene, L. E.; Johnson, J. C.; Saykally, R.; Yang, P., *Nat. Mater.* **2005**, *4*, 455–459.
14. Jang, Y. H.; Xin, X.; Byun, M.; Jang, Y. J.; Lin, Z.; Kim, D. H., *Nano. Lett.* **2011**, *12*, 479–485.
15. Brown, M. D.; Suteewong, T.; Kumar, R. S.; D'Innocenzo, V.; Petrozza, A.; Lee, M. M.; Wiesner, U.; Snaith, H. J., *Nano. Lett.* **2011**, *11*, 438–445.
16. Wu, W. Q.; Xu, Y. F.; Rao, H. S.; Feng, H. L.; Su, C. Y.; Kuang, D. B., *Angew. Chem., Int. Ed.* **2014**, *53*, 4816–4821.
17. Pan, J. H.; Wang, X. Z.; Huang, Q.; Shen, C.; Koh, Z. Y.; Wang, Q.; Engel, A.; Bahnemann, D. W., *Adv. Funct. Mater.* **2014**, *24*, 95–104.
18. Shiu, J. W.; Lan, C. M.; Chang, Y. C.; Wu, H. P.; Huang, W. K.; Diao, E. W. G., *ACS. Nano.* **2012**, *6*, 10862–10873.
19. Wang, W. G.; Zhang, H. Y.; Wang, R.; Feng, M.; Chen, Y. M., *Nanoscale* **2014**, *6*, 2390–2396.
20. Ye, M.; Xin, X.; Lin, C.; Lin, Z., *Nano. Lett.* **2011**, *11*, 3214–3220.
21. Wu, W. Q.; Xu, Y. F.; Su, C. Y.; Kuang, D. B., *Energy Environ. Sci.* **2014**, *7*, 644–649.
22. Chen, D. H.; Huang, F. Z.; Cheng, Y. B.; Caruso, R. A., *Adv. Mater.* **2009**, *21*, 2206–2210.
23. Selçuk, S.; Selloni, A., *J. Phys. Chem. C* **2013**, *117*, 6358–6362.
24. Yang, W.; Li, J.; Wang, Y.; Zhu, F.; Shi, W.; Wan, F.; Xu, D., *Chem. Commun.* **2011**, *47*, 1809–1811.
25. Yu, J.; Low, J.; Xiao, W.; Zhou, P.; Jaroniec, M., *J. Am. Chem. Soc.* **2014**, *136*, 8839–8842.
26. Ng, J.; Xu, S. P.; Zhang, X. W.; Yang, H. Y.; Sun, D. D., *Adv. Funct. Mater.* **2010**, *20*, 4287–4294.
27. Etgar, L.; Moehl, T.; Gabriel, S.; Hickey, S. G.; Eychmuller, A.; Gratzel, M., *ACS. Nano.* **2012**, *6*, 3092–3099.

28. Qian, J. F.; Liu, P.; Xiao, Y.; Jiang, Y.; Cao, Y. L.; Ai, X. P.; Yang, H. X., *Adv. Mater.* **2009**, *21*, 3663–3667.
29. Xu, C. K.; Wu, J. M.; Desai, U. V.; Gao, D., *Nano. Lett.* **2012**, *12*, 2420–2424.
30. Chandiran, A. K.; Nazeeruddin, M. K.; Gratzel, M., *Adv. Funct. Mater.* **2014**, *24*, 1615–1623.
31. Luo, J. S.; Karuturi, S. K.; Liu, L.; Su, L. T.; Tok, A. I. Y.; Fan, H. J., *Sci. Rep.* **2012**, *2*, NO.451.
32. Li, Y.; Wang, H.; Feng, Q.; Zhou, G.; Wang, Z. S., *Energy Environ. Sci.* **2013**, *6*, 2156–2165.
33. Wrighton, M. S.; Ellis, A. B.; Wolczanski, P. T.; Morse, D. L.; Abrahamson, H. B.; Ginley, D. S., *J. Am. Chem. Soc.* **1976**, *98*, 2774–2779.
34. Ng, J.; Xu, S.P.; Zhang, X.W.; Yang, H.Y.; Sun, D. D., *Adv. Funct. Mater.* **2010**, *20*, 4287–4296.
35. Huang, J. R.; Tan, X.; Yu, T.; Zhao, L.; Hu, W. L., *Electrochim. Acta* **2014**, *146*, 278–287.
36. Liu, Y. X.; Wang, Z. L.; Wang, W. D.; An, X. Q.; Mi, S. Y.; Tang, J. W.; Huang, W. X., *Appl. Surf. Sci.* **2014**, *315*, 314–322.
37. Zhu, Y. F.; Xu, L.; Hu, J.; Zhang, J.; Du, R. G.; Lin, C. J., *Electrochim. Acta* **2014**, *121*, 361–368.
38. Huang, J.R.; Tan, X.; Yu, T.; Zhao, L.; Xue S. Hu, W.L., *J. Mater. Chem. A* **2014**, *2*, 9975–9981.
39. Zhu, Y.F.; Xu, L.; Hu, J.; Zhang, J.; Du, R.C.; Lin, C.J., *Electrochim. Acta* **2014**, *121*, 361–368
40. Cao, T. P.; Li, Y. J.; Wang, C. H.; Shao, C. L.; Liu, Y. C., *Langmuir* **2011**, *27*, 2946–2952.
41. Kim, C. W.; Suh, S. P.; Choi, M. J.; Kang, Y. S.; Kang, Y. S., *J. Mater. Chem. A* **2013**, *1*, 11820–11827.
42. Zhang, Y.; Lin, S.; Zhang, W.; Ge, H.; Li, G.; Zhang, Y.; Qi, F. Y.; Song, X. M., *RSC. Adv.*, **2014**, *4*, 3226–3232.
43. Zhang, J.; Bang, J. H.; Tang, C. C.; Kamat, P. V., *ACS. Nano.* **2010**, *4*, 387–395.
44. Diamant, Y.; Chen, S. G.; Melamed, O.; Zaban, A., *J. Phys. Chem. B* **2003**, *107*, 1977–1981.
45. Wu, S. J.; Gao, X. S.; Qin, M. H.; Liu, J. M.; Hu, S. J., *Appl. Phys. Lett.* **2011**, *99*, 042106.
46. Han, X. G.; Kuang, Q.; Jin, M. S.; Xie, Z. X.; Zheng, L. S., *J. Am. Chem. Soc.* **2009**, *131*, 3152–3153.
47. Palomares, E.; Clifford, J. N.; Haque, S. A.; Lutz, T.; Durrant, J. R., *J. Am. Chem. Soc.* **2003**, *125*, 475–482.
48. Ito, S.; Chen, P.; Comte, P.; Nazeeruddin, M. K.; Liska, P.; Pechy, P.; Gratzel, M., *Prog. Photovolt: Res. Appl.* **2007**, *15*, 603–612.
49. Snaith, H. J., *Energy Environ. Sci.* **2012**, *5*, 6513–6520.
50. Tsumura, T.; Sogabe, K.; Toyoda, M., *Mater. Sci. Eng. B* **2009**, *157*, 113–115.
51. Walton, R. I.; Norquist, A.; Smith, R. I.; O'Hare, D., *Faraday Discuss.* **2003**, *122*, 331–341.
52. Qi, L.; Lee, B. I.; Badheka, P.; Yoon, D.H.; Samuels, W. D.; Exarhos, G. J., *J. Eur. Ceram. Soc.* **2004**, *24*, 3553–3557.
53. LaMer, V. K.; Dinegar, R. H., *J. Am. Chem. Soc.* **1950**, *72*, 4847–4854.
54. Ng, J.; Xu, S.; Zhang, X.; Yang, H. Y.; Sun, D. D., *Adv. Funct. Mater.* **2010**, *20*, 4287–4294.
55. Bai, H.; Liu, Z.; Sun, D. D., *Phys. Chem. Chem. Phys.* **2011**, *13*, 6205–6210.
56. Sanjinés, R.; Tang, H.; Berger, H.; Gozzo, F.; Margaritondo, G.; Lévy, F., *J. Appl. Phys.* **1994**, *75*, 2945–2951.
57. Aas, N.; Pringle, T. J.; Bowker, M., *J. Chem. Soc., Faraday Trans.* **1994**, *90*, 1015–1022.
58. Yang, W. D., *J. Mater. Sci.* **1999**, *34*, 3533–3544.
59. Longo, C.; Nogueira, A. F.; De Paoli, M. A.; Cachet, H., *J. Phys. Chem. B* **2002**, *106*, 5925–5930.
60. Wang, Q.; Ito, S.; Grätzel, M.; Fabregat-Santiago, F.; Mora-Seró, I.; Bisquert, J.; Bessho, T.; Imai, H., *J. Phys. Chem. B* **2006**, *110*, 25210–25221.
61. Yu, J.; Li, Q.; Shu, Z., *Electrochim. Acta* **2011**, *56*, 6293–6298.
62. Yoshida, Y.; Tokashiki, S.; Kubota, K.; Shiratuchi, R.; Yamaguchi, Y.; Kono, M.; Hayase, S., *Energy Mater. Sol. Cells* **2008**, *92*,

646–650.

63. Hoshikawa, T.; Yamada, M.; Kikuchi, R.; Eguchi, K., *J. Electrochem. Soc.* **2005**, *152*, E68–E73.

64. Han, L.; Koide, N.; Chiba, Y.; Mitate, T., *Appl. Phys. Lett.* **2004**, *84*, 2433–2335.

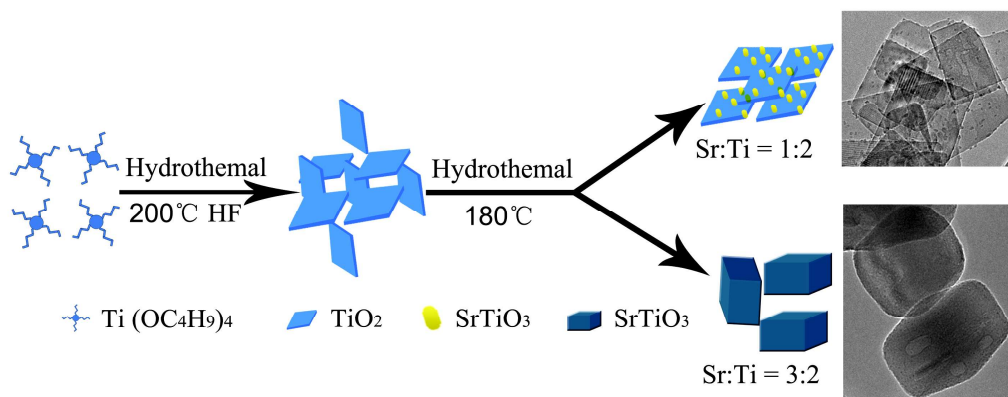
65. Park, J. T.; Roh, D. K.; Patel, R.; Kim, E.; Ryu, D. Y.; Kim, J. H., *J. Mater. Chem.* **2010**, *20*, 8521–8530.

66. Assmann, E.; Blaha, P.; Laskowski, R.; Held, K.; Okamoto, S.; Sangiovanni, G., *Phys. Rev. Lett.* **2013**, *110*, NO. 078701.

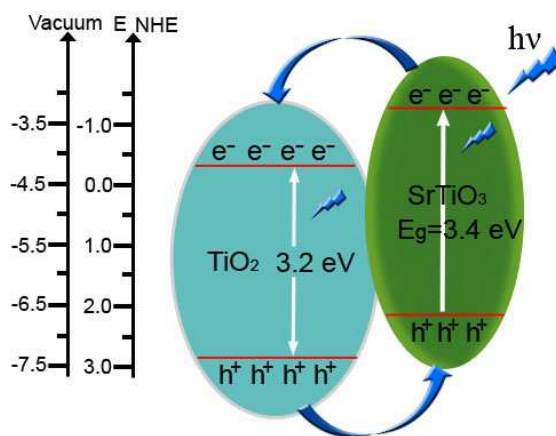
67. Matsutani, A.; Zhu, W.; Pezzotti, G., *J. Am. Ceram. Soc.* **2010**, *93*, 265–271.

68. Yue, X.Y.; Zhang, J.Y.; Yan, F.P.; Wang, X.; Huang, F. *Appl. Surface Sci.* **2014**, 319, 68-74.

## Figure Captions



**Scheme 1** Schematic illustration of the preparation process of the SrTiO<sub>3</sub>/TiO<sub>2</sub> heterostructure nanocrystals.



**Scheme 2** Schematic illustration of the proposed charge transfer process in SrTiO<sub>3</sub>/TiO<sub>2</sub> heterostructure under UV light irradiation.

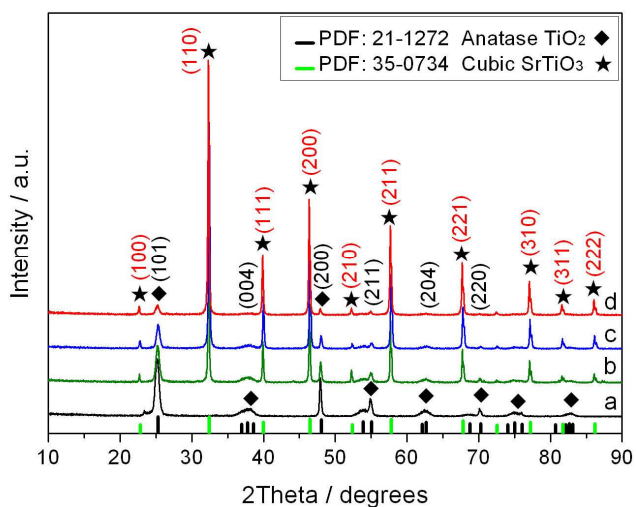


**Figure 1** XRD patterns of the as-prepared TiO<sub>2</sub> nanosheets and SrTiO<sub>3</sub>/TiO<sub>2</sub> heterostructure samples synthesized in different Sr/Ti molar ratios: (a) T1, (b) ST1, (c) ST2 and (d) ST3.

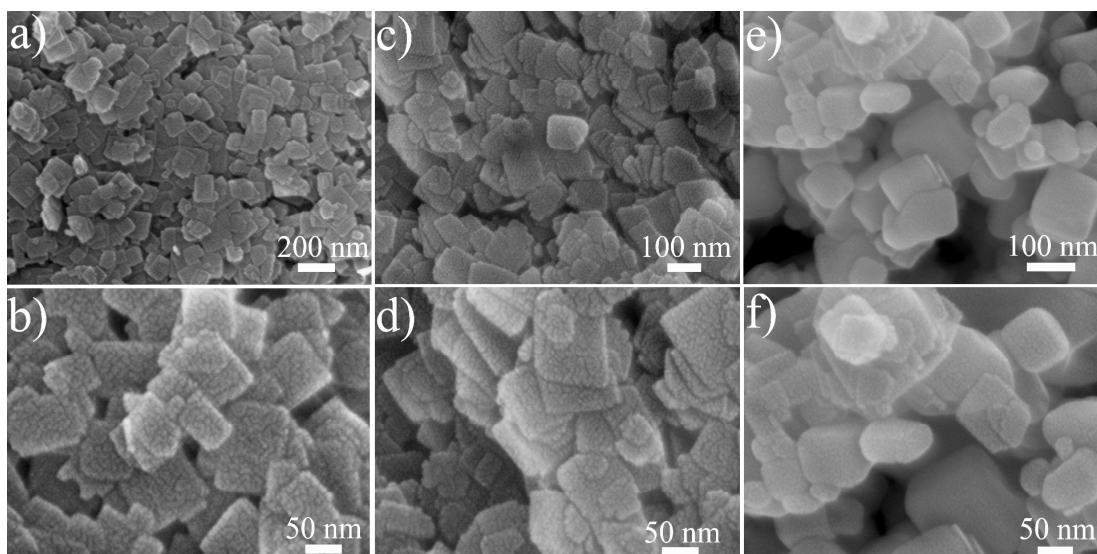


Figure 2 FE-SEM images of the as-prepared  $\text{TiO}_2$  nanosheets and the  $\text{SrTiO}_3/\text{TiO}_2$  samples synthesized in different Sr/Ti molar ratios:

(a) (b) T1, (c) (d) ST1, (e) (f) ST3.

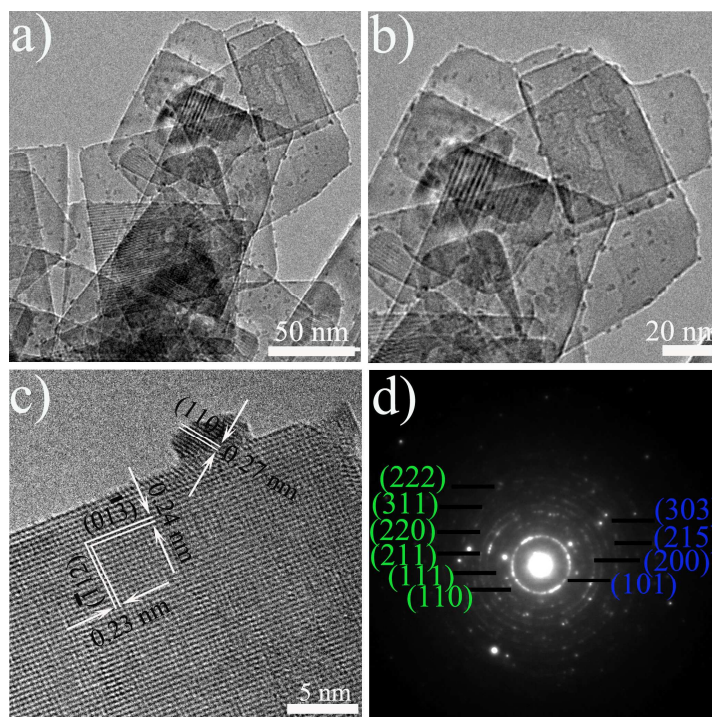


Figure 3 (a) TEM image of ST1 sample. (b) Magnified TEM image of ST1 sample. (c) HRTEM lattice image of ST1 sample. The marked d-spacing of 0.27 nm for a nanoparticle is in well agreement with that of (110) plane of cubic  $\text{SrTiO}_3$ , while the marked d-spacing of 0.23 nm and 0.24 nm corresponds well with d-spacing of (-112) and (01-3) planes of anatase  $\text{TiO}_2$ , respectively. (d) Electron diffraction pattern reveals the phase components of the ST1 samples, the diffraction rings corresponding well with that of (101), (200), (215), (303) planes of anatase  $\text{TiO}_2$ , and (110), (111), (211), (220), (311), (303) planes of cubic  $\text{SrTiO}_3$ .

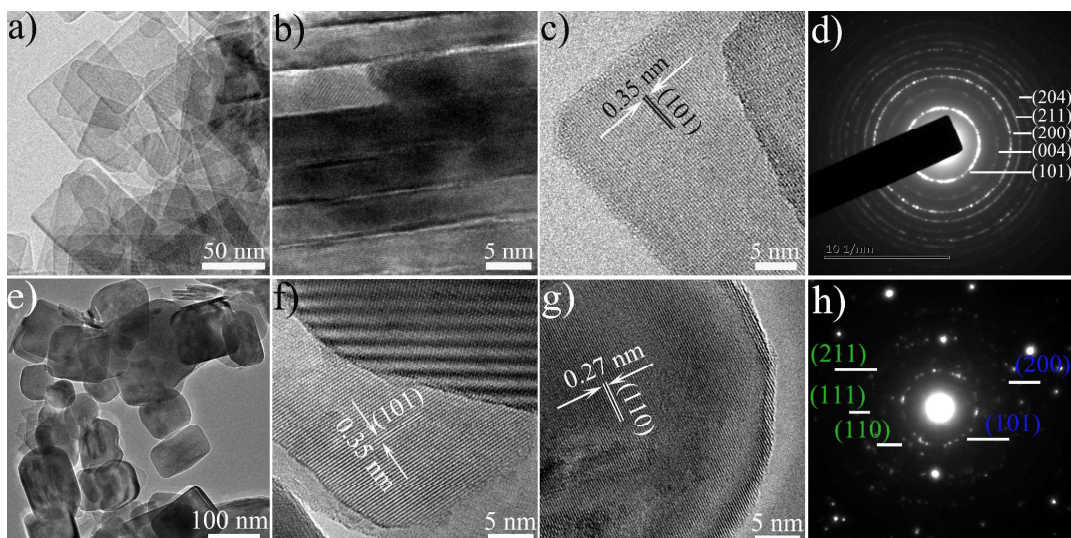


Figure 4 (a) (b) Low magnification TEM images of T1 sample. (c) A typical HRTEM lattice image and (d) Electron diffraction pattern for T1 sample. (e) Low magnification TEM image of ST3 sample. (f) (g) HRTEM lattice images, the fringe spacing of 0.35 nm in Fig. 4f corresponds to d-spacing of (101) plane of anatase  $\text{TiO}_2$  nanosheet, while the fringe spacing of 0.27 nm in Fig. 4g matches well with d-spacing of (110) plane of cubic  $\text{SrTiO}_3$ . (h) ED pattern clearly shows that the ST3 sample is composed of cubic  $\text{SrTiO}_3$  and anatase  $\text{TiO}_2$ , with diffraction rings corresponding well with (101), (200) planes of anatase  $\text{TiO}_2$ , and (110), (111), (211) planes of cubic  $\text{SrTiO}_3$ , respectively.

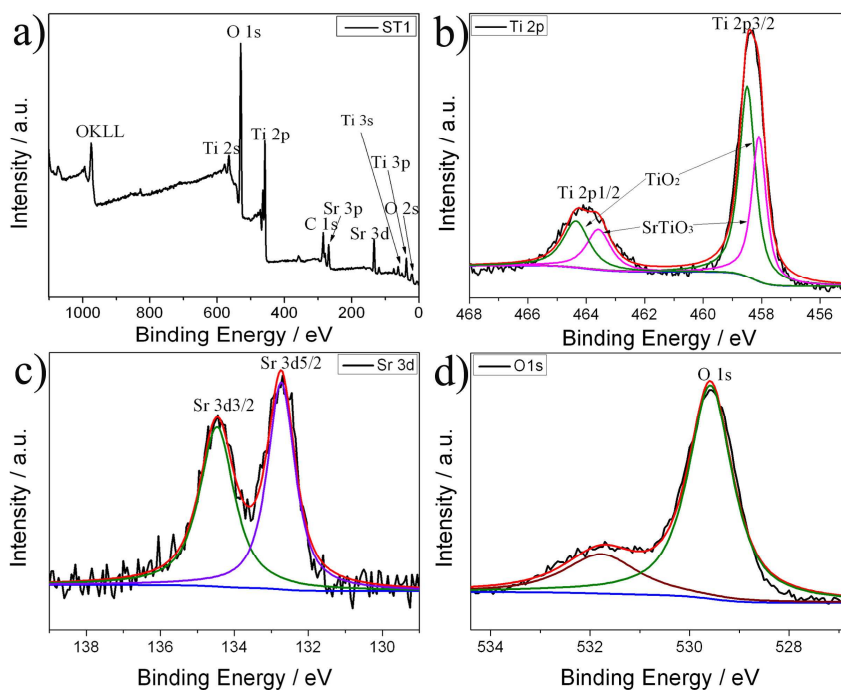


Figure 5 (a) XPS survey spectra. High-resolution XPS spectrum of (b) Ti 2p, (c) Sr 3d, and (d) O 1s of the ST1 sample.

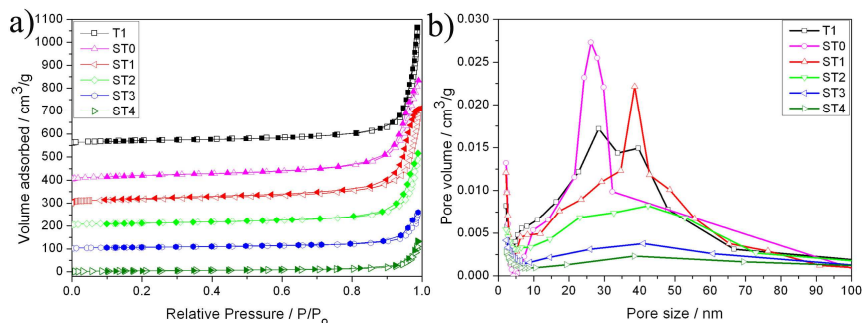


Figure 6 (a) N<sub>2</sub> adsorption-desorption curves. (b) Pore size distribution plot for the as-prepared TiO<sub>2</sub> nanosheets and the SrTiO<sub>3</sub>/TiO<sub>2</sub> samples (open symbols: adsorption; closed symbols: desorption).

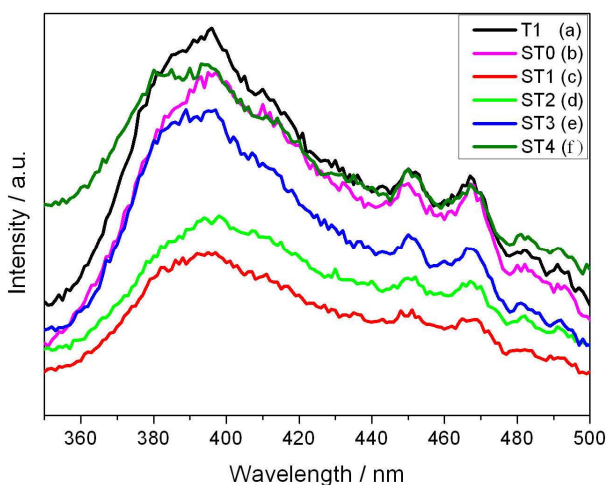


Figure 7 PL spectra of (a) T1, (b) ST0, (c) ST1, (d) ST2, (e) ST3 and (f) ST4 samples.

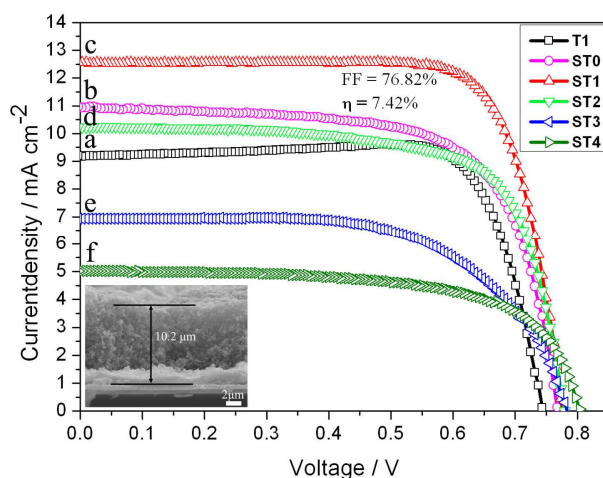


Figure 8 J-V curves of DSSCs based on samples of (a) T1, (b) ST0, (c) ST1, (d) ST2, (e) ST3 and (f) ST4. (Inset) a cross-sectional FESEM image of SrTiO<sub>3</sub>/TiO<sub>2</sub> heterostructures (ST1) film on the FTO layer by the spin coating method.

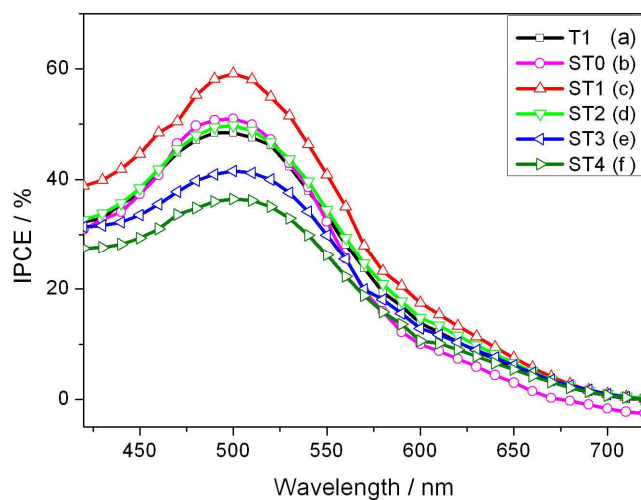


Figure 9 IPCE spectra of DSSCs based on samples of (a) T1, (b) ST0, (c) ST1, (d) ST2, (e) ST3 and (f) ST4.

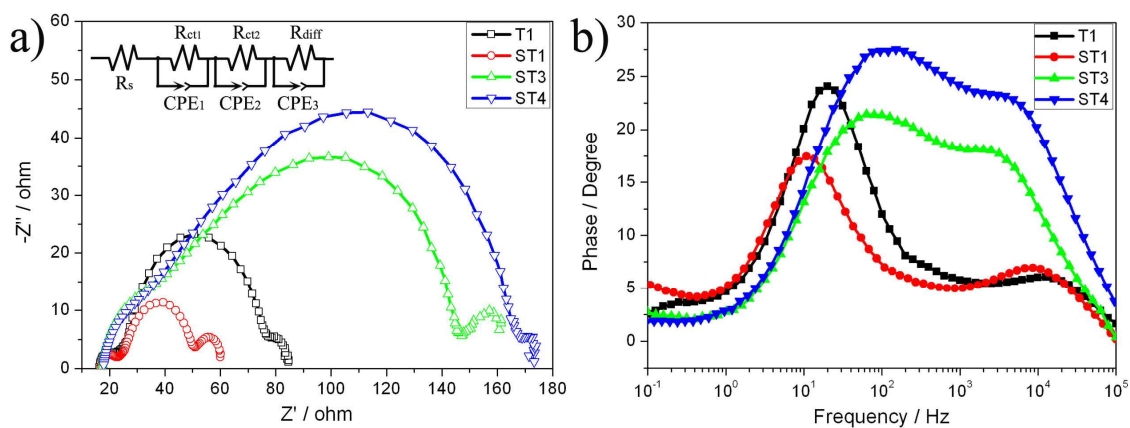


Figure 10 Impedance spectra of DSSCs based on T1, ST1, ST3 and ST4 photoanodes measured at  $V_{oc}$  under illumination of  $100 \text{ mW cm}^{-2}$ : (a) Nyquist plots, with the inset showing the equivalent circuit, and (b) Bode phase plots.

For Table of Contents

